

Early detection of pulmonary arterial hypertension through [¹⁸F] positron emission tomography imaging with a vascular endothelial receptor small molecule

Zhen Yang¹ | Feng Li¹ | Rajarajan A. Thandavarayan²  | Kartiga Natarajan³ | Diego R. Martin^{1,4} | Zheng Li^{1,5} | Ashrith Guha²

¹Department of Radiology, Houston Methodist Academic Institute, Houston, Texas, USA

²Department of Cardiology, Houston Methodist Hospital, Houston, Texas, USA

³Department of Cardiovascular Sciences, Houston Methodist Research Institute, Houston, Texas, USA

⁴Department of Radiology, Weil Cornell Medicine, New York, New York, USA

⁵Center for Scientific Review, NIH, Bethesda, Maryland, USA

Correspondence

Ashrith Guha, 6550 Fannin St, Suite 1901, Houston, TX 77030, USA.

Email: gashrith@houstonmethodist.org

Zheng Li, 6701 Rockledge Dr, Bethesda, MD 2081, USA.

Email: zheng.li3@nih.gov

Funding information

Houston Methodist Academic Institute (HMAI), Blake and Roswell Vaughan Research Fund and HMAI Foundation; MD Anderson Foundation Distinguished Endowed Chair

Abstract

The objective of this study is to provide a positron emission tomography (PET) imaging modality targeting vascular endothelial growth factor receptors (VEGFR) for the early noninvasive detection and assessment of pulmonary arterial hypertension (PAH) severity. To validate the effectiveness of the [¹⁸F] VEGFR PET tracer, we utilized a monocrotaline (MCT)-induced PAH rat model. Molecular optical imaging, using a Cy5.5-conjugated VEGFR targeting agent, was employed to demonstrate the uptake of the agent at pulmonary arterioles, correlating with the onset and progression of PAH. Histological examinations of the MCT-PAH rat lung revealed a significant correlation between VEGFR2 expression and the pathogenesis of PAH. Molecular optical imaging demonstrated heightened uptake of the Cy5.5-conjugated VEGFR targeting agent at pulmonary arterioles, corresponding with the onset and progression of PAH. [¹⁸F]VEGFR PET showed increased lung uptake detectable in early-stage PAH before increase in pulmonary artery pressures, and this uptake correlated with increased PAH severity. Moreover, when compared to [¹⁸F]FDG PET, [¹⁸F]VEGFR PET exhibited markedly lower background cardiac signal, enhancing imaging sensitivity for lung abnormalities. Our study provides a compelling evidence for the potential utility of the innovative [¹⁸F]VEGFR PET tracer, in non-invasively detecting early signs of PAH, and monitoring its progression. The observed correlations between VEGFR2 expression, molecular optical imaging results, and [¹⁸F]VEGFR PET findings support the use of this tracer for early detection, and assessment of PAH severity. The lower background cardiac signal observed with [¹⁸F]VEGFR PET further enhances its imaging sensitivity, emphasizing its potential clinical significance.

KEYWORDS

[¹⁸F]VEGFR, early stage-PAH, PET imaging, pulmonary artery

Zhen Yang and Feng Li are joint first authors.

This is an open access article under the terms of the [Creative Commons Attribution-NonCommercial](https://creativecommons.org/licenses/by-nc/4.0/) License, which permits use, distribution and reproduction in any medium, provided the original work is properly cited and is not used for commercial purposes.

© 2024 The Author(s). *Pulmonary Circulation* published by John Wiley & Sons Ltd on behalf of Pulmonary Vascular Research Institute.

INTRODUCTION

Pulmonary arterial hypertension (PAH) is a progressive condition characterized by vascular remodeling, leading to narrowing of small pulmonary arterioles, leading to an increase in the vascular resistance.¹⁻⁴ PAH is associated with a 5-year mortality rate of 50%, with an average delay of 2.2 years from symptom onset to diagnosis.⁵⁻⁷ Majority of patients are diagnosed at an advanced NYHA functional class (III or greater), primarily because of the delay in diagnosis. In most cases 70% of the pulmonary vascular reserve has been lost by the time of diagnosis, leading to an irreversible trajectory of this disease.^{5,6} Data from multinational PAH registries suggests that an early diagnosis of PAH and early therapeutic intervention can result in an improved long-term survival rate.⁸⁻¹⁰ In addition, almost 50% of patients have underlying diseases such as connective tissue disease, portopulmonary hypertension, and HIV which account for more than 50% of all incident PAH cases.¹¹ Hence, there is an urgent need to develop a clinically useful noninvasive tool that can detect early pathophysiological changes associated with PAH and enable earlier diagnosis. Such a tool could prove beneficial in early disease diagnosis in patients at risk of developing PAH, including those with connective tissue disease and familial PAH. The current gold standard for diagnosis is heart catheterization, which is invasive and tends to be reserved for symptomatic patients. Furthermore, the clinical diagnosis of PAH relies on identification of late manifestation of the disease, that is, increase in mean pulmonary artery pressure (mPAP), but not by the identification of the underlying pathophysiological process.

Pathogenesis of PAH is characterized by abnormal vascular remodeling, due to increased proliferation of endothelial, smooth muscle and adventitial cells. Increased expression of vascular endothelial growth factor (VEGF) receptor 2 in smooth muscle cells and endothelium, along with elevated VEGF levels, results in medial hypertrophy and intimal hyperplasia of the pulmonary arterioles.^{2,12-16} Hence there is the potential opportunity of VEGFR molecular imaging to quantify lung vascular remodeling, and for early detection of the pathological changes associated with PAH. This study endeavors to establish a robust noninvasive imaging tool for the early detection of PAH, utilizing a rodent monocrotaline (MCT) model.

To achieve this objective, we successfully developed a small-molecule agent, diZD, derived and modified from the antiangiogenic drug ZD6474 (vandetanib). Subsequently, we radiolabeled diZD with ¹⁸F to create a novel [¹⁸F] VEGFR PET tracer for PAH, outlining the radiolabeling

process for the first time in this report. Following the synthesis, we investigated the biodistribution and specificity of [¹⁸F] diZD binding to VEGFR. Our study extends to the *in vivo* and *in vitro* evaluation of the [¹⁸F]VEGFR PET tracer's performance, aiming to assess disease severity and establish its utility as an early detection tool for PAH.

Furthermore, we conducted a comparative analysis between [¹⁸F]VEGFR PET and the widely available [¹⁸F] FDG PET to discern their detective performance in detecting vascular changes associated with PAH. This comprehensive exploration of the [¹⁸F]VEGFR PET tracer, from synthesis to evaluation, forms a critical step toward advancing our understanding of its potential as a sensitive and specific imaging modality for early-stage PAH detection.

MATERIALS AND METHODS

Animal model

MCT induced PAH rat model was employed to investigate the pathophysiology of PAH as we described earlier.¹⁷ Briefly, 2-month-old Sprague Dawley rats obtained from Charles River, USA, were subjected to a single intraperitoneal injection of monocrotaline (60 mg/kg) dissolved in dimethyl sulfoxide (DMSO). Following the injection, the rats were maintained on a standard diet and observed during the 2nd and fourth weeks post-MCT administration to monitor the progressive development of PAH. This assessment involved the analysis of hemodynamic parameters and histological characteristics of lung tissues. In alignment with this study's designations, rats at the conclusion of the second week were categorized as being in the "early stage of PAH," while those at the end of the 4th week were designated as being in the "late stage of PAH." The same rats subjected to MCT-induced PAH were also used for the subsequent imaging studies. All animal experimentation was conducted in accordance with approved protocols, adhering to the guidelines established by the Institutional Animal Care and Use Committee of the Houston Methodist Research Institute (IACUC No: IS00004103).

Measurement of right ventricular systolic pressures (RVSPs)

The method for determining RVSPs followed established procedures as we described earlier.¹⁷ In brief, the heart was accessed through a midline thoracotomy under deep anesthesia in an oxygen-enriched environment (100% O₂). Utilizing a high-fidelity catheter tip transducer (Mikro-Tip SPR-671) from Millar Instruments, direct recordings of

right ventricle (RV) pressures were obtained. The catheter was inserted into the RV for this purpose. The analysis was conducted after achieving a stable state, confirmed by at least 10 s of continuous measurements, and the results were averaged for accuracy.

Optical imaging

For the optical imaging study, 20 nmol Cy5.5-diZD reconstituted in 0.5 mL physiological phosphate-buffered saline (PBS) was intravenously injected into the MCT-PAH rats through tail vein 30 min before the imaging scan. Fluorescence imaging was captured at excitation wavelength of 670 nm and the emission at 720 nm using a PerkinEler IVIS Spectrum. Healthy rats (no MCT exposure), PAH rats of early stage (second week after MCT exposure) and PAH rats of late stage (fourth week after MCT exposure) were studied and compared in the optical imaging study. To overcome the limitation of the optical signal in the tissue penetration depth, animals were euthanized, and the chest surgically opened to expose the lungs. This facilitated imaging by making the fluorescence signal emitted from the lungs superficially detectable. In addition, a blocking study was performed by adding 1 μ mol diZD (no Cy5.5 conjugation) as a competing agent in the injected formula; this was conducted in the imaging study of late-stage PAH rats. After completing animal imaging, major organs and tissue, including blood, heart, lung, liver, kidney, spleen, gastrointestinal, and muscle, were collected and optically imaged using standardized imaging conditions for determining the relative biodistribution of the Cy5.5-diZD imaging probe. Regions of interest were drawn to quantify fluorescence intensity emitted from the uptake probe in the lungs. Afterwards the lung samples were frozen and sliced into 4–5 μ m slides; the slides were subjected to hematoxylin and eosin (H&E) histological staining, for morphology, and imaging of the *in vivo* uptake probe was performed using a fluorescence microscope. Six rats per group were used for statistical comparison.

Micro positron emission tomography/computed tomography (PET/CT) imaging

Small-animal PET/CT scans were performed and analyzed using a Siemens Inveon PET/CT imaging system. For [18 F]VEGFR-PET imaging, [18 F]AIF-NOTA-diZD (~37 MBq, 1 mCi, 0.35 nmol per rat) was intravenously injected into the rats via the tail vein. Afterward, in-line CT and PET scans were collected at 1 h postinjection.

Images were obtained using the manufacturer's two-dimensional (2D) and three-dimensional (3D) ordered-subsets expectation maximum algorithm (Siemens). The obtained scans were reconstructed and processed using the manufacturer's software platform (Inveon, Siemens). The radioisotope concentration (accumulation) within tissue was expressed as counts per milliliter per minute, converted to counts per gram per minute, assuming a tissue density of 1 g mL⁻¹, and lastly normalized by injected dose (ID) as percentage of the injected dose per gram of tissue (% ID/g).

We also performed comparative PET imaging for PAH detection, using [18 F]FDG PET imaging, on rats injected with [18 F]FDG. Briefly, rats were fasted and fed only with water 6 h before the imaging study. [18 F]FDG (~37 MBq, 1 mCi per rat) was intravenously injected into rats via the tail vein. The PET/CT imaging was performed at 1 h post injection and the images were processed accordingly.

To validate specific binding of the probe, a blocking experiment was performed by coinjection of [18 F]AIF-NOTA-diZD with 100-fold nonradioactive diZD (~35 nmol) into rats at 4 weeks after MCT injection. The imaging protocol in the blocking study were the same as described above. In total, four groups, six animals per group, were studied by imaging, including healthy rats (Control group), rats exposed to MCT for 2 weeks (early-stage PAH group), rats exposed to MCT for 4 weeks (late-stage PAH group) and a blocking study group were compared.

Biodistribution study

The biodistribution *ex vivo* study was performed on tissues harvested immediately following the *in vivo* PET imaging study in the MCT-PAH rats. Specifically, major organs and tissues were collected, including blood, RV, left ventricle (LV), lung, liver, kidney, spleen, gut (GI), and muscle. The wet weight of each tissue specimen and the radioactivity was measured using a 2470 Wizard2 Automatic Gamma Counter (PerkinElmer). The radio-tracer distribution among the organs was calculated as radioactivity divided by tissue wet-weight and the decay-corrected injected dose, to derive the % ID/g ratio. The biodistribution study was performed on each of the animals and in all of the four study groups.

Histology

Histological studies were performed on the collected rat lungs fixation in 4% formaldehyde immediately after harvesting, for 24 h, then processed and embedded in a

wax block, which was sliced into 4–5 μm sections for further analysis. For morphology staining, the lung tissue sections were stained with H&E, according to the manufacturer's instructions. For the VEGFR2 antibody staining, serial sections were deparaffinized in xylene, and then rehydrated through a solution gradient of 100% ethanol, 95% ethanol, 70% ethanol, and water. The rehydrated slides were treated with 0.3% hydrogen peroxide for 20 min, followed by incubation in 5% horse serum for 30 min to block nonspecific binding of the primary antibody. Then, sections were stained with VEGFR2 antibody (Rabbit mAb, 1:1000 dilution). Detection was performed with an horseradish peroxidase (HRP)-conjugated respective secondary system followed by diaminobenzidine and counter-staining with a hematoxylin solution. Images were captured using an inverted microscope.

Human samples and immunohistochemical staining (IHC) staining

Human lung tissues underwent a parallel histology assessment, including samples from both normal individuals and those diagnosed with PAH. These tissues were sourced from our institutional biobank, and the entire process was carried out in compliance with internal review board guidelines and human research retrospective study protocols. For the scope of this study, exclusively recent cases were chosen in a randomized manner. This selection was predicated on a retrospective search within pathology reports, enabling the selection of lung tissues representing both normal conditions and moderately advanced histological features characteristic of PAH. Lung tissues were fixed in formalin, embedded in paraffin blocks, and sectioned for IHC staining. Briefly, sections were deparaffinized, rehydrated, and treated with 0.3% hydrogen peroxide as described previously, and to retrieve antigen, slides were incubated in Tris HCL buffer (pH 9.0) at 100°C for 10 min. Then sections were stained with VEGFR2 antibody (1:400) overnight, followed by ImmPRESS HRP Horse Anti-Rabbit IgG Polymer secondary antibody system from Vector laboratory (MP-7401) for 30 min. Signals were detected using a liquid 3'-diaminobenzidine + substrate chromogen system from DAKO (K3468), counterstained with hematoxylin, and images were captured using Olympus AX70 microscope.

Materials and reagents

VEGFR2 antibody (VEGF Receptor 2 Rabbit mAb #2479) was purchased from Cell Signaling Technology. NOTA-

NHS-Ester was purchased from Macrocyclics. [^{18}F] Sodium fluoride aqueous solution was provided by Cyclotope Radiopharmacy. Water was purified using a Milli-Q ultra-pure water system from Millipore. The targeting agent, diZD, was synthesized as previously described.^{18–20} H&E stain kit (catalog# IW-3100) was commercially obtained from IHC World. All other reagents and solvents were purchased from Sigma-Aldrich and used without further purification unless otherwise stated.

Synthesis of Cy5.5-diZD

0.2 mL diZD dissolved in DMSO solution (10 $\mu\text{mol}/\text{mL}$) was mixed with Cy5.5 mono NHS ester (2.5 mg, 2.2 μmol) in 0.6 mL DMSO in the dark at ambient temperature. After stirring overnight in the dark at room temperature, the reaction was quenched by adding 200 μL trifluoroacetic acid (TFA). Purification of the crude product was carried out on a semipreparative reversed-phase high-performance liquid chromatography (HPLC) system (Agilent 1200 series). Phenomenex Luna C18(2) column 100R (250 \times 10.00 mm) was used. The flow was set 4 mL/min with the mobile phase starting from 70% solvent A (0.05 M ammonia acetate in water) and 30% solvent B (acetonitrile) to 50% solvent A and 50% solvent B at 20 min. The analytic HPLC method was performed with the same gradient system but replaced with Phenomenex Luna C18(2) column 100R (250 \times 4.6 mm) and flow rate of 1 mL/min. The absorbance was monitored at 254 and 675 nm. The peak containing the Cy5.5-diZD product was collected, dissolved in dimethyl sulfoxide (DMSO) and reconstituted to 10 $\mu\text{mol}/\text{mL}$ solution and stored in the dark at -20°C for further use. The MS spectrum of Cy5.5-diZD was: m/z 1055.51 (100, $[\text{M} + 2\text{H}]^{2+}$, calculated 105.22); 654.11, $[\text{M} + 3\text{H}]^{3+}$.

Synthesis of NOTA-diZD

NOTA-diZD was synthesized for the subsequent F-18 radiolabeling. Briefly, NOTA-NHS-Ester (3 mg, 6 μmol) was added to 0.5 mL 10 $\mu\text{mol}/\text{mL}$ diZD DMSO solution, followed by addition of 50 μL triethylamine. The reaction mixture was stirred in the dark at ambient temperature overnight and then quenched by adding 200 μL of triethylamine. The crude product was purified by a semipreparative reversed-phase HPLC employing a Phenomenex Luna C-18 column (250 \times 10 mm) with the mobile phase 70% solvent A (0.1% TFA in water) and 30% solvent B (acetonitrile), and the flow rate was 5 mL/min. Fractions containing NOTA-diZD were collected,

lyophilized, re-dissolved in DMSO at a concentration of 10 $\mu\text{mol/mL}$, and stored in the dark at -20°C until use. The purified NOTA-diZD was characterized by mass spectroscopy (MS). MS (electrospray): m/z 1523.39 ($[\text{M} + \text{H}]^{+}$, calculated 1523.27); 762.50 ($[\text{M} + 2\text{H}]^{2+}$); 509.04 ($[\text{M} + 3\text{H}]^{3+}$).

Radiolabeling of $[\text{}^{18}\text{F}]\text{AIF-NOTA-diZD}$

The following reagents were added into 1.5 mL reaction tube to constitute reaction mixture: 100 μL acetonitrile, 5 μL AlCl_3 (2 mM in 0.1 sodium acetate buffer at pH 4), 2.5 μL NOTA-diZD (10 mM in DMSO), 45 mCi $[\text{}^{18}\text{F}]\text{NaF}$ in 200 μL saline. The reaction mixture was incubated at 100°C for 15 min. The reaction was terminated by addition of 200 μL metal-free water, and then the crude mixture was purified with a semi-preparative HPLC. Chemical structure of NOTA-diZD and $[\text{}^{18}\text{F}]\text{AIF-NOTA-diZD}$ was shown in Supporting Information: Scheme S1. The fraction containing $[\text{}^{18}\text{F}]\text{AIF-NOTA-diZD}$ was collected and measured radioactivity of 16–18 mCi. The solvent was removed using a C18 cartridge. The final product was recollected and constituted into PBS for in vivo injection. The radioactive yield was about $37.5 \pm 2.5\%$ (nondecay correction), and the specific activity was around 2.8 mCi/nmol. Stability of $[\text{}^{18}\text{F}]\text{AIF-NOTA-diZD}$ was examined by radio-HPLC after incubating the $[\text{}^{18}\text{F}]\text{AIF-NOTA-diZD}$ at mouse serum at 37°C for 4 h and compared with the freshly purified $[\text{}^{18}\text{F}]\text{AIF-NOTA-diZD}$ (shown in Supporting Information: Figure S1).

Statistics

The quantitative data was expressed as mean \pm SD. Differences between groups and the control groups were assessed by the Student *t*-test using GraphPad Prism (9.2.0) software. A 95% confidence level was chosen to determine significance between compared groups, with *p*-values of less than 0.05 indicating significant differences.

RESULTS

Stages of the MCT-PAH rats

Figure 1 shows the RVSP measurements along with a histological evaluation of the MCT-PAH rat model used in this study. Figure 1a shows healthy rats treated with vehicle, as a control, retained a normal RVSP of 24 ± 9 mmHg. Rats exposed to MCT for 2 weeks (early stage PAH) had an RVSP of 26 ± 7 mmHg, which was

statistically not different from control animals. After exposure to MCT for 4 weeks (late-stage PAH), a significant increase in RVSP was noted with a mean of 73 ± 10 mmHg when compared with the control group. Histological examination of the lung tissue revealed the onset and progression of MCT-induced PAH (Figure 1b). The pulmonary arterioles in the early-stage PAH group revealed medial thickening, and histological changes which were significant compared to the “control” rats. In late-stage PAH the pulmonary arterioles exhibited severe vessel wall hypertrophy and obstruction of the lumen which was confirmed by semi-quantitative analysis of vessel lumen fraction which progressively decreased as the stage progressed.

Optical imaging for MCT-PAH rats

We first synthesized an optical probe from a VEGFR targeting small molecule, diZD, which was previously developed in our lab.¹⁸⁻²¹ The targeting agent was conjugated with Cy5.5 fluorescence dye to perform optical imaging of MCT-PAH rats at Weeks 2 and 4. Figure 2 shows the optical VEGFR imaging of MCT-PAH rats. Due to the limited penetration depth of optical imaging, animals were euthanized, and the chest opened surgically to expose lung surface tissue and to allow for optical fluorescence imaging acquisitions at 30 min postinjection of VEGFR-targeting agent Cy5.5-diZD.

Region of interest (ROI) analysis of lung in the optical imaging showed uptake of Cy5.5-diZD was significantly increased in the early phase PAH rats when compared to the control rats ($*p < 0.05$), even though there was no significant difference in the RVSP between the groups. As the PAH progressed, the lung uptake of the Cy5.5-diZD increased further in the late stage PAH rats ($***p < 0.001$). Cocktail of excessive blocking agent significantly decreased the lung signal in the VEGFR optical imaging suggesting excellent specificity.

Histology of MCT-PAH lung

Lung tissue from the VEGFR optical imaging of MCT-PAH rats was collected for histological study and biochemical assays. Figure 3a shows the H&E stained morphology and fluorescence images acquired at the cellular level of the lung tissue from the VEGFR optical imaging of MCT-PAH rats. Medial thickening and vessel lumen obliteration were mild and severe in the early and late-stage PAH lungs, respectively. The fluorescence images acquired at the cellular level showed a specific accumulation of the

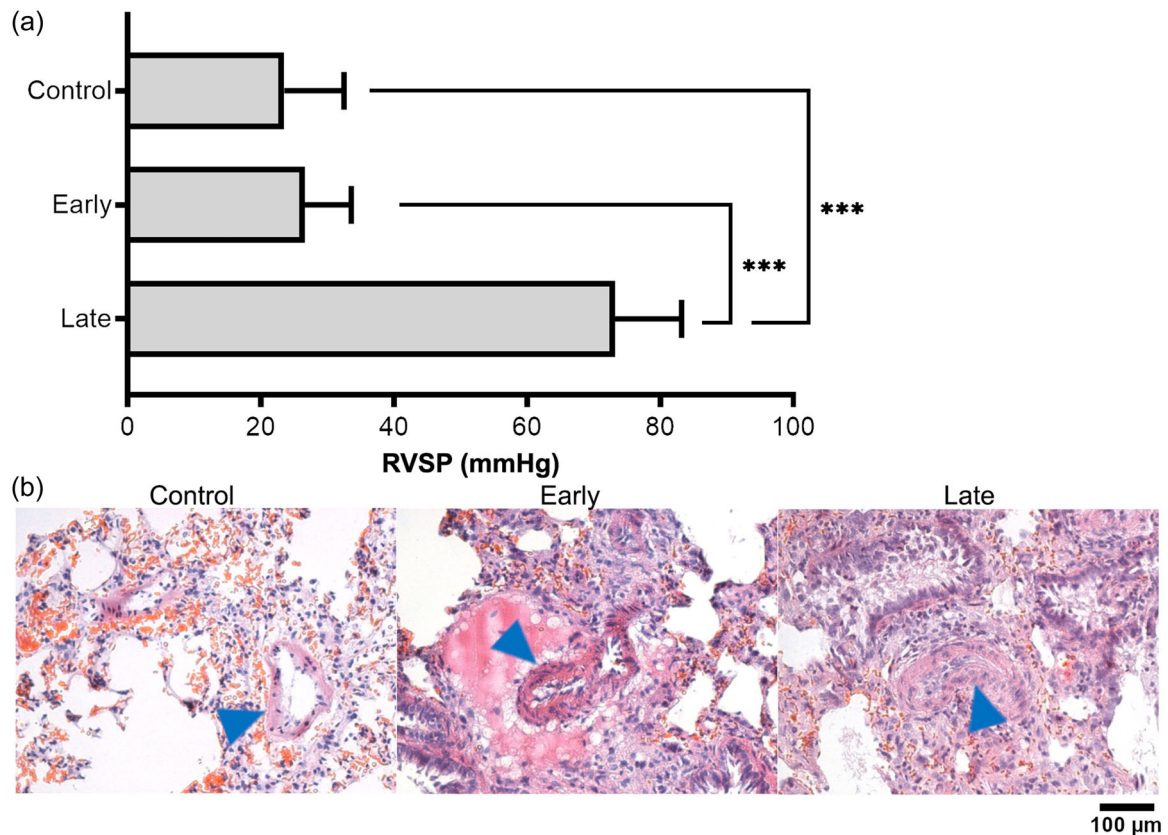


FIGURE 1 The PAH status of the experimental MCT-PAH rats was confirmed by (a) measurement of right ventricular systolic pressure (RVSP, measured as the mean pulmonary arterial pressure in mmHg), and (b) H&E histological staining of rat lung for vascular remodeling in pulmonary arteries and arterioles. Rats at various levels of MCT exposure were studied: “Control” (healthy rats without MCT exposure), “Early” (rats exposed to MCT for 2 weeks) and “Late” (rats exposed to MCT for 4 weeks). Blue triangles mark the pulmonary arteries and arterioles. Six rats per group were used for statistical analysis. The representative histology demonstrates a normal *Control* arterial wall (b, left photomicrograph) with progressive wall thickening, infiltrates, and sclerosis evolving from *Early* (b, middle photomicrograph) to *Late* (b, right photomicrograph). H&E, hematoxylin and eosin; MCT, monocrotaline; PAH, pulmonary arterial hypertension.

Cy5.5-diZD probe at the pulmonary arterioles and arteries. Remarkably, the fluorescence intensities, as quantified in Figure 3b, revealed a positive correlation with the PAH progression and optical imaging results in Figure 2. The lung tissue was also examined using anti-VEGFR2 IHC (Figure 3c) and western blot analysis (Figure 3d). The IHC result clearly showed positive VEGFR2 expression at pulmonary arterioles and arteries, and the expression increased significantly as remodeling progressed. Upregulation of VEGFR2 was confirmed with the western blot analysis of proteins extracted from the lungs of both early and late-stage PAH lungs.

VEGFR PET imaging of MCT-PAH rats

Since optical imaging confirmed our initial hypothesis, diZD molecule was radiolabeled with ^{18}F for [^{18}F]VEGFR

PET imaging. Its chemical structure was shown as Supporting Information: Scheme S1. Figure 4 shows the transverse view of the lungs in the in vivo PET imaging of MCT-PAH rats. [^{18}F]FDG PET and [^{18}F]diZD PET imaging were performed in parallel on four groups of rats (early stage, late stage PAH, control, and blocking group) and compared. [^{18}F]diZD PET showed significant uptake in early PAH rats in lung field when compared to control, and the lung uptake of the [^{18}F]diZD PET tracer was much more in late-stage PAH. Significant glucose uptake was observed in the lungs on [^{18}F]FDG PET scans of late stage PAH animals. However, there was no significant difference in the lung uptake of early stage PAH and control animals on [^{18}F]FDG PET scans. In addition, high background uptake of FDG could interfere with the interpretation of lung uptake in the [^{18}F]FDG PET, whereas [^{18}F]diZD PET exhibited low interference uptake in the background.

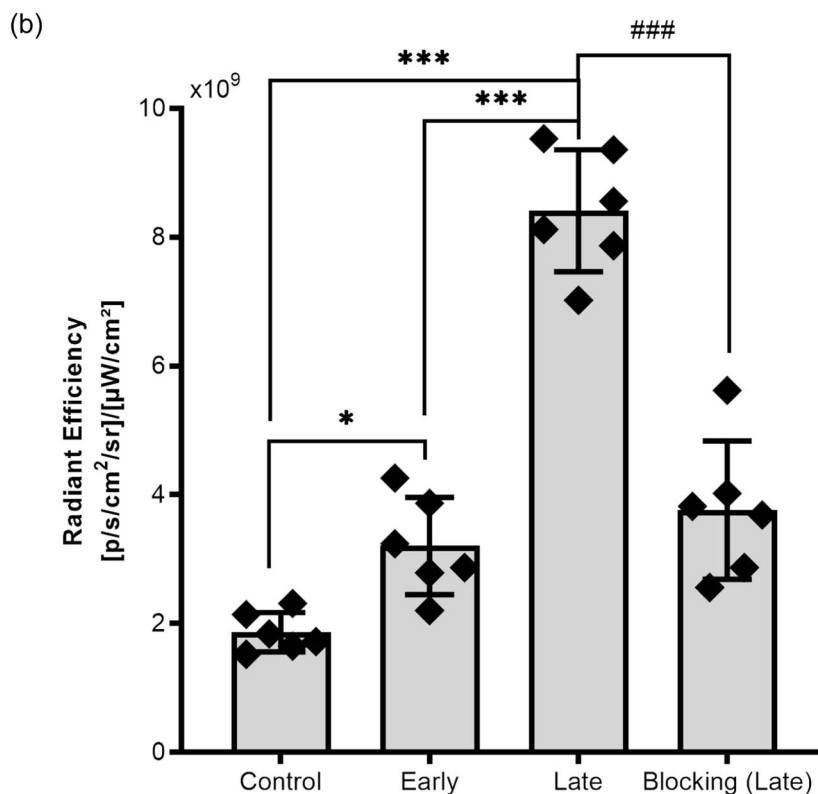
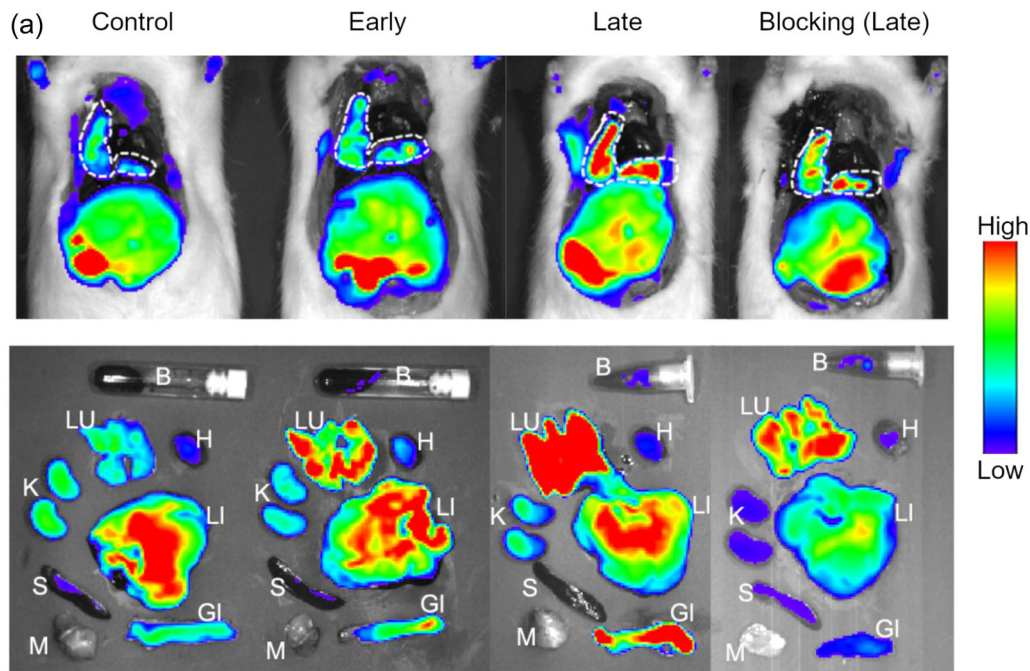


FIGURE 2 (a) Optical imaging of MCT-PAH rats using Cy5.5-diZD probe and (b) ROI quantification of lung uptake of the probe. Major organs and tissue, including blood (B), lung (LU), heart (H), liver (LI), kidney (K), spleen (S), gut (GI), and muscle (M), were collected for biodistribution study. Rats at different stages of PAH were studied: “Control” (healthy rats without MCT exposure), “Early” (rats exposed to MCT for 2 weeks), and “Late” (rats exposed to MCT for 4 weeks). In addition, a blocking imaging study was also performed at “Late” MCT-PAH rats as “Blocking” group. Dashed white line circled the lungs in the animal images. Six rats per group were used for statistical analysis. MCT, monocrotaline; PAH, pulmonary arterial hypertension; ROI, region of interest.

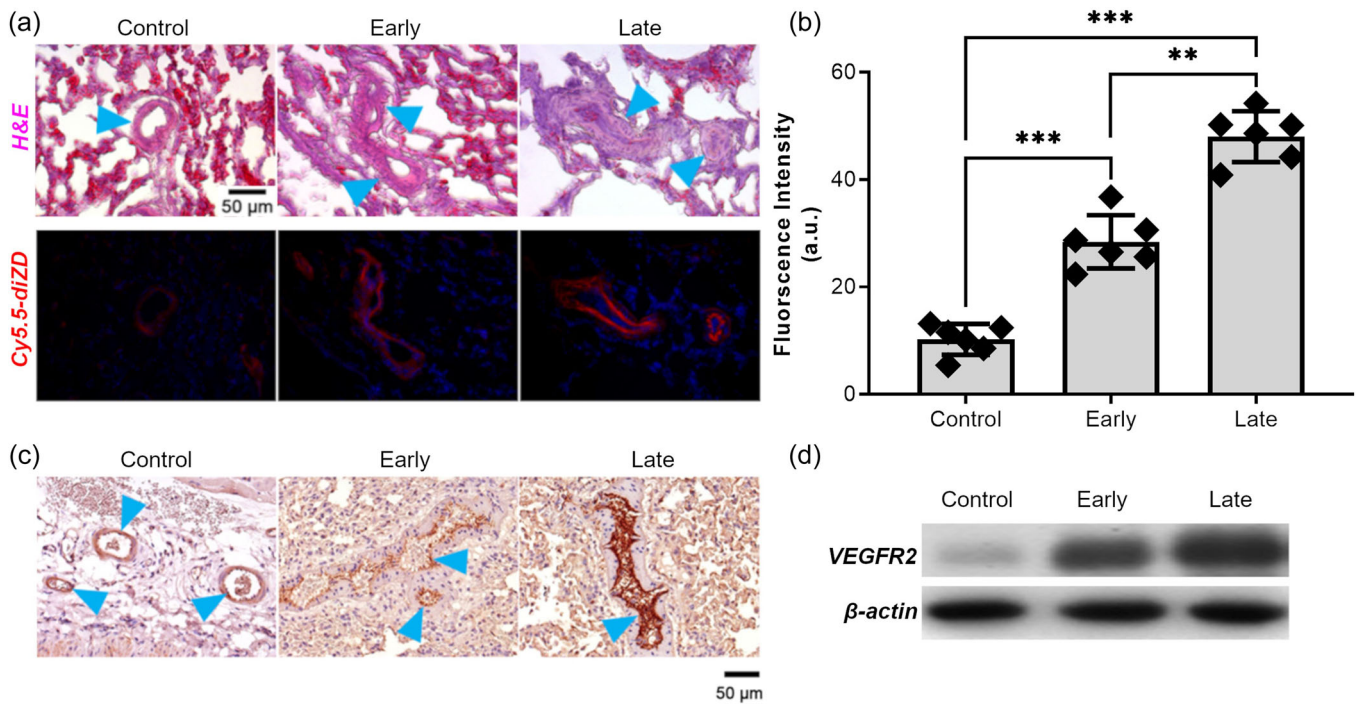


FIGURE 3 Histological study of MCT-PAH lungs. (a) H&E staining and fluorescence imaging of PAH lungs collected from the optically imaged rats. (b) fluorescence intensities in (a) were quantified and compared across groups of “Control”, “Early,” and “Late” as defined in the optical imaging study. (c) IHC staining using anti-VEGFR2 antibody was performed to examine the VEGFR expression in the MCT-PAH lungs. (d) Rat lungs harvested from another cohort of MCT-PAH rats were lysed, and the proteins were extracted and then performed western blot analysis to examine its VEGFR2 expression. H&E, hematoxylin and eosin; IHC, immunohistochemistry; MCT, monocrotaline; PAH, pulmonary arterial hypertension; VEGFR, vascular endothelial growth factor receptors.

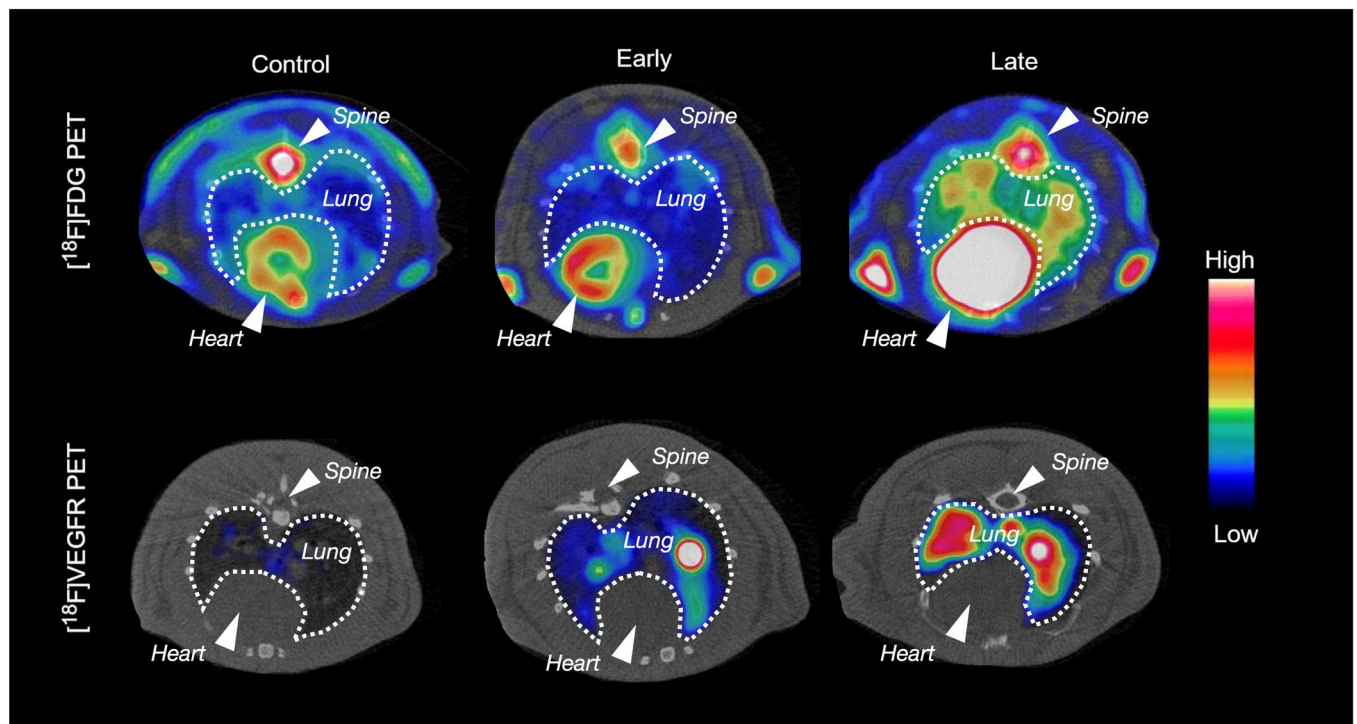


FIGURE 4 In vivo $[^{18}\text{F}]\text{FDG}$ and $[^{18}\text{F}]\text{VEGFR}$ PET/CT imaging of MCT-PAH rats shown as transverse views of the lung. Rats at various levels of MCT exposure were studied: “Control” (healthy rats without MCT exposure), “Early” (rats exposed to MCT for 2 weeks) and “Late” (rats exposed to MCT for 4 weeks). Six rats per group were used. Lungs were outlined with white dashed line, and the heart and spine indicated with white arrows. MCT, monocrotaline; PAH, pulmonary arterial hypertension; PET/CT, positron emission tomography/computed tomography; VEGFR, vascular endothelial growth factor receptors.

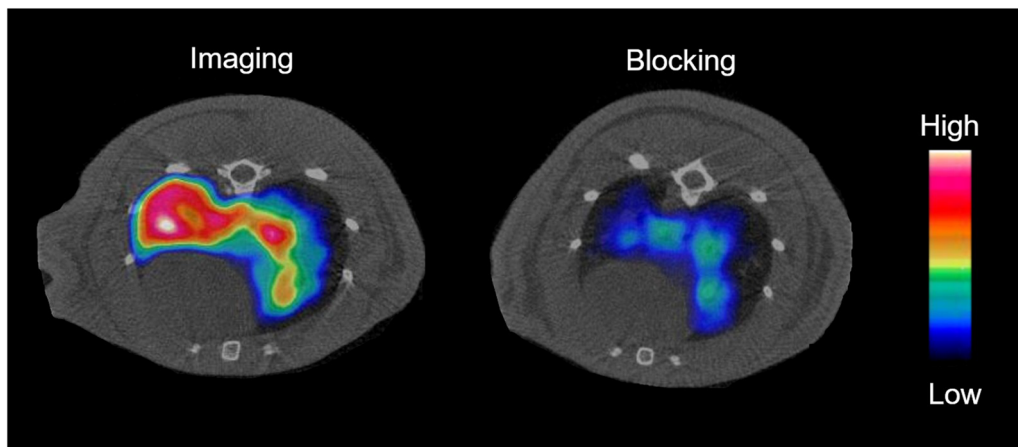


FIGURE 5 Blocking study on the [^{18}F]VEGFR PET imaging of MCT-PAH rats. “Late” PAH rats were used, and two groups were compared: “Imaging” (imaging using [^{18}F]VEGFR PET tracer only), “Blocking” (imaging using [^{18}F]VEGFR PET tracer supplemented with excessive non-radiolabeled “cold” VEGFR-targeting agent, diZD). Six rats per group were used. MCT, monocrotaline; PAH, pulmonary arterial hypertension; PET, positron emission tomography; VEGFR, vascular endothelial growth factor receptors.

To validate the specificity of [^{18}F]diZD PET to PAH, a typical blocking study using cocktail of [^{18}F]AlF-NOTA-diZD and excessive non-radio labeled diZD as blocking agent was performed on late-stage PAH animals. Figure 5 shows transverse view of the lungs in the *in vivo* PET imaging vs blocking of MCT-PAH rats. The lung uptake of [^{18}F]diZD PET tracer was significantly decreased in the blocked group when compared with the late-stage PAH group.

Biodistribution

The biodistribution of [^{18}F]FDG PET and [^{18}F]diZD PET tracer among major organs are depicted in Figure 6. In general, the residual activity of [^{18}F]diZD PET tracer in all the metabolic organs, including liver, kidney, and gut, were all less than 1%ID/g after 1 h administration, whereas the activity in the MCT lungs remained commensurately high. In addition, we further investigated the tracers uptake among right and left ventricles in the [^{18}F]diZD PET and [^{18}F]FDG PET. In [^{18}F]diZD PET, uptake in the heart is very low, no distinguishable tracer uptake was observed in right ventricle among control and early stage PAH, late stage PAH exhibited a small increase but statistically significant increase when compared to controls. As for the uptake in left ventricle, neither the “Early,” or the “Late” PAH showed a differentiable pattern in [^{18}F]diZD PET. Notably, the uptake of [^{18}F]diZD PET tracer in the right ventricle was significantly reduced in the “Blocking” rats, corresponding to the lung uptake

pattern. For [^{18}F]FDG PET, we found both right and left ventricles showed correlative increase of [^{18}F]FDG uptake in the “Early” and “Late” PAH.

Histology of human lung PAH

To assess the clinical applicability of this tracer in humans, we conducted immunohistochemistry on human lung tissues to investigate the potential elevation of VEGFR2 expression in PAH. Figure 7 demonstrates minimal VEGFR2 levels in healthy lung tissue, while a substantial upregulation of VEGFR2 was noted in the lung tissue from a PAH patient, characterized by pronounced abnormal vascular remodeling consistent with PAH histological features.

DISCUSSION

In our study, using the MCT-PAH rat model, we found that activation of the vascular remodeling via the VEGF pathway appears to be detectable through PET imaging earlier than increase in RVSP. Furthermore, [^{18}F]diZD PET signal intensity in lungs appears to increase with the worsening of PAH. Our findings are in keeping with PAH pathophysiology based upon vascular remodeling with up regulation of vascular growth factors and increased expression of receptors, including VEGFR. These findings are consistent with histological changes seen in PAH, including angiogenesis and proliferation of pulmonary arteriole endothelial and mural cells, including

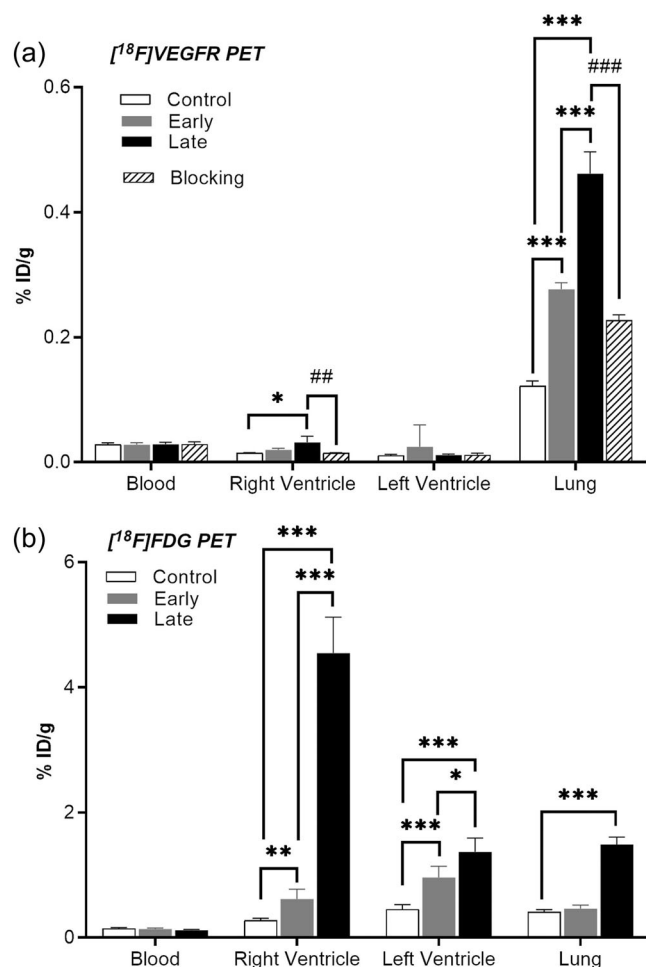


FIGURE 6 (a–b) Biodistribution study of $[^{18}\text{F}]\text{VEGFR PET}$ and $[^{18}\text{F}]\text{FDG PET}$ among major organs. Rats at various levels of MCT exposure were studied: “Control” (healthy rats without MCT exposure), “Early” (rats exposed to MCT for 2 weeks), and “Late” (rats exposed to MCT for 4 weeks). For $[^{18}\text{F}]\text{VEGFR PET}$, additional “Blocking” group was also studied. Six rats per group were used. MCT, monocrotaline; PAH, pulmonary arterial hypertension; PET, positron emission tomography; VEGFR, vascular endothelial growth factor receptors.

smooth muscle and subendothelial matrix, leading to luminal narrowing or occlusion.

Our findings strongly suggest a role for VEGFR PET imaging in PAH, as shown by the VEGFR tracer, $[^{18}\text{F}]\text{diZD}$ binding observed in both ex vivo and in vivo lung imaging using optical fluorescence and radiotracer PET imaging studies. Moreover, the histological examination of cellular uptake of the VEGFR-targeting agent, Cy5.5-diZD, supported its specific accumulation at pulmonary arterioles, which underlay the vascular-remodeling pathogenesis of PAH. PAH is associated with increased endothelial leaking, hence raising the question of nonspecific accumulation of DiZD.²² Marked decrease

in VEGFR uptake in blocking experiments show that the tracer binding was specific to VEGF Receptor 2.

The diagnostic potential of $[^{18}\text{F}]\text{diZD PET}$ for noninvasive detection of PAH was compared to $[^{18}\text{F}]\text{FDG PET}$ for early and late stages of PAH. $[^{18}\text{F}]\text{FDG PET}$ has been used in the clinical evaluation of PAH, but with inconsistent results.^{8,23} In our study, only “late” PAH stage manifested increased uptake of $[^{18}\text{F}]\text{FDG}$, whereas no detectable uptake of $[^{18}\text{F}]\text{FDG}$ was observed in early PAH. Strong background uptake of $[^{18}\text{F}]\text{FDG}$ also poses a challenge to sensitivity for detection of early changes of PAH. In addition variability with heterogeneity in lung $[^{18}\text{F}]\text{FDG}$ uptake in PAH patients has been reported, including variation resulting from drugs that attenuate $[^{18}\text{F}]\text{FDG}$ uptake through improved oxidative phosphorylation.^{23–25} These factors potentially limit the clinical applicability of $[^{18}\text{F}]\text{FDG PET}$ for early detection of PAH. Importantly $[^{18}\text{F}]\text{diZD PET}$, developed here, addressed the above issues, showing higher sensitivity for early PAH with markedly lower background uptake in heart or lung.

Potential limitations of our study include validation of the animal model used. For the past two decades, the MCT rat model has contributed to a better understanding of vascular remodeling in PAH.^{17,26} This model provides technical simplicity, reproducibility, and low cost and it continues to be frequently employed for the study of PAH. To validate the in vivo PET imaging and tracer distribution of $[^{18}\text{F}]\text{VEGFR}$, we showed the expected and similar tracer lung uptake using alternative optical-fluorescence ex vivo and in vivo experiments, and we showed uptake of tracer in the pulmonary arterioles on fluorescence microscopy.

Our study also includes preliminary evidence of clinical relevance with findings of elevated VEGFR expression in the human lung tissue of a patient with PAH, compared to normal human lung that shows less detectable background VEGFR. Although a comprehensive evaluation of human lung tissues was outside the scope of this study, our findings show such a study is warranted. The marked increase of VEGFR2 expression, from a very low basal level at healthy state to a highly positive level early in the development of PAH, before detectability by conventional clinical methods, supports a potential diagnostics role for clinical application using, for example, $[^{18}\text{F}]\text{diZD PET}$ for PAH early detection. Questions remain whether VEGFR is a specific biomarker for PAH across the various etiological subtypes or if this biomarker is elevated in other non-PAH lung diseases. Further investigation of human lung specimens is warranted to further delineate the clinical utility of $[^{18}\text{F}]\text{diZD PET}$ tracer.

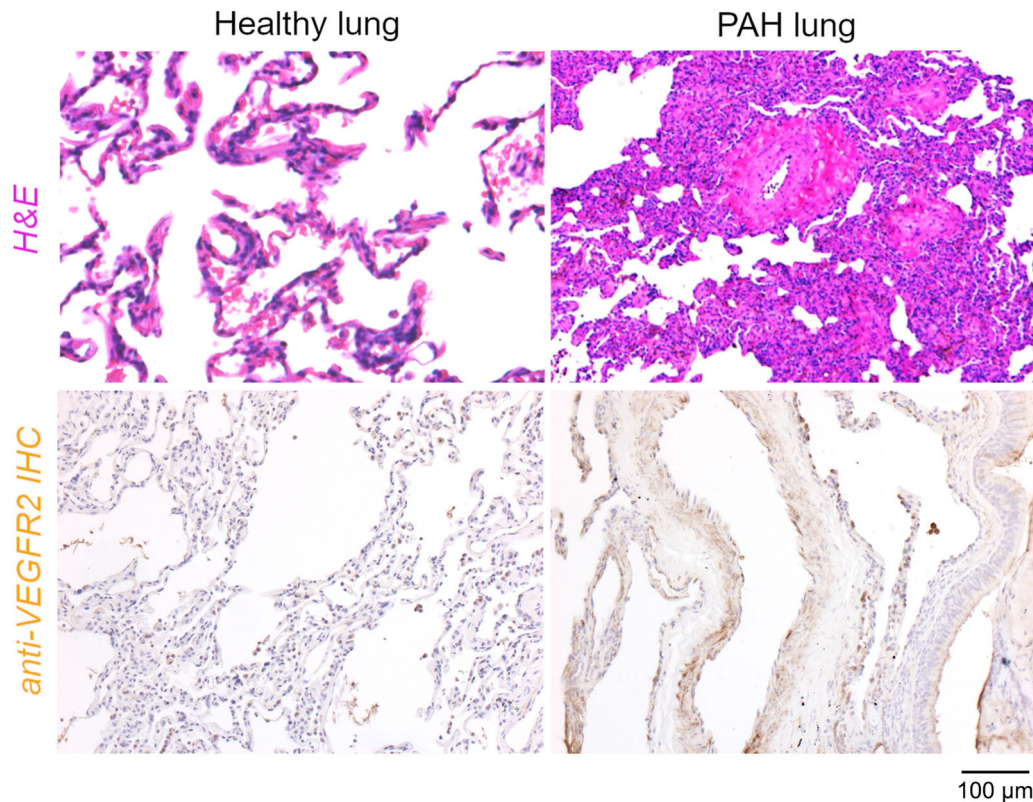


FIGURE 7 Human lung H&E and VEGFR2 immunohistochemistry (IHC) stained tissues from histologically classified normal control “Healthy” and “PAH” patient specimens. There is marked arteriole hypertrophy characteristic of advanced PAH. Minimal VEGFR2 levels in healthy lung tissue, while a substantial upregulation of VEGFR2 was noted in the lung tissue from a PAH patient, characterized by pronounced abnormal vascularization consistent with PAH histological features. H&E, hematoxylin and eosin; PAH, pulmonary arterial hypertension; VEGFR, vascular endothelial growth factor receptors.

CONCLUSION

We identified VEGFR as a sensitive biomarker associated with pathogenic onset and development of PAH in the MCT-PAH rat model. Our findings are consistent with the molecular mechanism that angiogenesis is associated with PAH development and progression due to excessive proliferation of vascular wall cells in pulmonary arterioles. [^{18}F]diZD PET tracer developed in this study showed sensitivity for early and late stages of PAH and was able to differentiate early from late disease. Moreover, [^{18}F]diZD PET outperformed [^{18}F]FDG PET, which has been studied for its utility in PAH. The further translational importance of [^{18}F]diZD PET for clinical management of PAH has to be studied.

AUTHOR CONTRIBUTIONS

Feng Li designed and synthesized the VEGFR2 targeting agent. Zhen Yang and Feng Li performed all the experiments. Rajarajan A. Thandavarayan helped with the pulmonary pressure measurement and Kartiga Natarajan performed IHC for VEGFR2 in human tissue sections. Zhen Yang and Feng Li drafted the manuscript.

Diego R. Martin, Zheng Li, Kartiga Natarajan, Rajarajan A. Thandavarayan, and Ashrith Guha revised the manuscript. The study was designed and supervised by Zheng Li and Ashrith Guha. Ashrith Guha is the guarantor of the content of the manuscript.

ACKNOWLEDGMENTS

This work was supported by the Houston Methodist Academic Institute (HMAI), Blake and Roswell Vaughan Research Fund, and HMAI Foundation. We thank Dr. Kimberly Greer for assistance in preparation of this manuscript and we also thank the preclinical imaging core facility of HMAI. This research was funded in part through the MD Anderson Foundation Distinguished Endowed Chair.

CONFLICT OF INTEREST STATEMENT

The authors declare no conflicts of interest.

DISCLAIMER


This work was prepared while Dr. Zheng Li was employed at Houston Methodist Hospital Research Institute. The opinions expressed in this article are the

author's own and do not reflect the view of the National Institutes of Health, the Department of Health and Human Services, or the United States government.

ETHICS STATEMENT

All animal experimentation was conducted in accordance with approved protocols, adhering to the guidelines established by the Institutional Animal Care and Use Committee of the Houston Methodist Research Institute (IACUC No: IS00004103).

ORCID

Rajarajan A. Thandavarayan  <http://orcid.org/0000-0001-8452-2903>

REFERENCES

1. Stenmark KR, McMurtry IF. Vascular remodeling versus vasoconstriction in chronic hypoxic pulmonary hypertension. *Circ Res.* 2005;97(2):95–8.
2. Siafakas NM, Antoniou KM, Tzortzaki EG. Role of angiogenesis and vascular remodeling in chronic obstructive pulmonary disease. *Int J Chronic Obstruct Pulm Dis.* 2007;2(4):453–62.
3. Humbert M, Morrell NW, Archer SL, Stenmark KR, MacLean MR, Lang IM, Christman BW, Weir EK, Eickelberg O, Voelkel NF, Rabinovitch M. Cellular and molecular pathobiology of pulmonary arterial hypertension. *J Am Coll Cardiol.* 2004;43(12 Suppl S):13s–24s.
4. Archer SL, Weir EK, Wilkins MR. Basic science of pulmonary arterial hypertension for clinicians: new concepts and experimental therapies. *Circulation.* 2010;121(18):2045–66.
5. Brown LM, Chen H, Halpern S, Taichman D, McGoon MD, Farber HW, Frost AE, Liou TG, Turner M, Feldkircher K, Miller DP, Elliott CG. Delay in recognition of pulmonary arterial hypertension. *Chest.* 2011;140(1):19–26.
6. Strange G, Gabbay E, Kermeen F, Williams T, Carrington M, Stewart S, Keogh A. Time from symptoms to definitive diagnosis of idiopathic pulmonary arterial hypertension: the delay study. *Pulm Circ.* 2013;3(1):89–94.
7. Hachulla E, Gressin V, Guillevin L, Carpentier P, Diot E, Sibilia J, Kahan A, Cabane J, Francès C, Launay D, Mouthon L, Allanore Y, Tiev KP, Clerson P, de Groote P, Humbert M. Early detection of pulmonary arterial hypertension in systemic sclerosis: a French nationwide prospective multicenter study. *Arthritis Rheum.* 2005;52(12):3792–800.
8. Lau EMT, Humbert M, Celermajer DS. Early detection of pulmonary arterial hypertension. *Nat Rev Cardiol.* 2015;12(3):143–55.
9. McGoon MD, Benza RL, Escribano-Subias P, Jiang X, Miller DP, Peacock AJ, Pepke-Zaba J, Pulido T, Rich S, Rosenkranz S, Suissa S, Humbert M. Pulmonary arterial hypertension: epidemiology and registries. *J Am Coll Cardiol.* 2013;62(25):D51–9.
10. Humbert M, Gerry Coghlan J, Khanna D. Early detection and management of pulmonary arterial hypertension. *Eur Respir Rev.* 2012;21(126):306–12.
11. Yancy CW, Jessup M, Bozkurt B, Butler J, Casey DE, Drazner MH, Fonarow GC, Geraci SA, Horwich T, Januzzi JL, Johnson MR, Kasper EK, Levy WC, Masoudi FA, McBride PE, McMurray JJV, Mitchell JE, Peterson PN, Riegel B, Sam F, Stevenson LW, Tang WHW, Tsai EJ, Wilkoff BL. 2013 ACCF/AHA guideline for the management of heart failure. *J Am Coll Cardiol.* 2013;62(16):e147–239.
12. Santos S, Peinado VI, Ramírez J, Morales-Blanhir J, Bastos R, Roca J, Rodriguez-Roisin R, Barberà JA. Enhanced expression of vascular endothelial growth factor in pulmonary arteries of smokers and patients with moderate chronic obstructive pulmonary disease. *Am J Respir Crit Care Med.* 2003;167(9):1250–6.
13. Voelkel NF, Gomez-Arroyo J. The role of vascular endothelial growth factor in pulmonary arterial hypertension: the angiogenesis paradox. *Am J Respir Cell Mol Biol.* 2014;51(4):474–84.
14. Farkas L, Farkas D, Ask K, Möller A, Gaudie J, Margetts P, Inman M, Kolb M. VEGF ameliorates pulmonary hypertension through inhibition of endothelial apoptosis in experimental lung fibrosis in rats. *J Clin Invest.* 2009;119(5):1298–311.
15. Pako J, Bikov A, Karlocai K, Csosza G, Kunos L, Losonczy G, Horvath I. Plasma VEGF levels and their relation to right ventricular function in pulmonary hypertension. *Clin Exp Hypertens.* 2015;37(4):340–4.
16. Säleby J, Bouzina H, Ahmed S, Lundgren J, Rådegran G. Plasma receptor tyrosine kinase RET in pulmonary arterial hypertension diagnosis and differentiation. *ERJ Open Res.* 2019;5(4):00037–2019.
17. Gomez-Arroyo JG, Farkas L, Alhussaini AA, Farkas D, Kraskauskas D, Voelkel NF, Bogaard HJ. The monocrotaline model of pulmonary hypertension in perspective. *Am J Physiol Lung Cell Mol Physiol.* 2012;302(4):L363–9.
18. Li F, Jiang S, Zu Y, Lee DY, Li Z. A tyrosine kinase inhibitor-based high-affinity PET radiopharmaceutical targets vascular endothelial growth factor receptor. *J Nucl Med.* 2014;55(9):1525–31.
19. Yang Z, Li F, Yelamanchili D, Zeng Z, Rosales C, Youker KA, Shen H, Ferrari M, Mahmarian J, Pownall HJ, Hamilton DJ, Li Z. Vulnerable atherosclerotic plaque imaging by small-molecule high-affinity positron emission tomography radiopharmaceutical. *Adv Ther.* 2019;2(8):1900005.
20. Freysoldt C, Merz P, Schmidt M, Mohitkar S, Felser C, Neugebauer J, Jansen M. Cover picture: discovery of elusive K4O6, a compound stabilized by configurational entropy of polarons. *Angew Chem Int Ed.* 2019;58(31):1.
21. Huang Y, Yang Z, Li F, Zhao H, Li C, Yu N, Hamilton DJ, Li Z. ⁶⁴Cu/¹⁷⁷Lu-DOTA-diZD, a small-molecule-based therapeutic pair for triple-negative breast cancer. *J Med Chem.* 2021;64(5):2705–13.
22. Zhou C, Francis CM, Xu N, Stevens T. The role of endothelial leak in pulmonary hypertension (2017 Grover Conference Series). *Pulm Circ.* 2018;8(4):1–9.
23. Ahmadi A, Ohira H, Mielniczuk LM. FDG PET imaging for identifying pulmonary hypertension and right heart failure. *Curr Cardiol Rep.* 2015;17:555.

24. Zhao L, Ashek A, Wang L, Fang W, Dabral S, Dubois O, Cupitt J, Pullamsetti SS, Cotroneo E, Jones H, Tomasi G, Nguyen QD, Aboagye EO, El-Bahrawy MA, Barnes G, Howard LS, Gibbs JSR, Gsell W, He JG, Wilkins MR. Heterogeneity in lung 18FDG uptake in pulmonary arterial hypertension. *Circulation*. 2013;128(11):1214–24.
25. Marsboom G, Wietholt C, Haney CR, Toth PT, Ryan JJ, Morrow E, Thenappan T, Bache-Wiig P, Piao L, Paul J, Chen CT, Archer SL. Lung 18F-fluorodeoxyglucose positron emission tomography for diagnosis and monitoring of pulmonary arterial hypertension. *Am J Respir Crit Care Med*. 2012;185(6):670–9.
26. Wilson DW, Segall HJ, Pan LC, Lamé MW, Estep JE, Morin D. Mechanisms and pathology of monocrotaline pulmonary toxicity. *Crit Rev Toxicol*. 1992;22(5–6):307–25.

SUPPORTING INFORMATION

Additional supporting information can be found online in the Supporting Information section at the end of this article.

How to cite this article: Yang Z, Li F, Thandavarayan RA, Natarajan K, Martin DR, Li Z, Guha A. Early detection of pulmonary arterial hypertension through [¹⁸F] positron emission tomography imaging with a vascular endothelial receptor small molecule. *Pulm Circ*. 2024;14:e12393. <https://doi.org/10.1002/pul2.12393>